


## PAPER



Cite this: *Nanoscale Adv.*, 2021, 3, 6468

# Visible light active Zr- and N-doped TiO<sub>2</sub> coupled g-C<sub>3</sub>N<sub>4</sub> heterojunction nanosheets as a photocatalyst for the degradation of bromoxynil and Rh B along with the H<sub>2</sub> evolution process†

Souman Pahi, Sumanta Sahu, Satish Kumar Singh, Abhijit Behera and Raj Kishore Patel \*

Herein, we drastically increased the light-harvesting abilities of TiO<sub>2</sub> by creating a defect level with doping using zirconium (Zr) and nitrogen (N). Titanium was substantially replaced by Zr from its lattice point, and N was bound on the surface as (NO)<sub>x</sub>. The doped system comes with a reduced band edge of 2.8 eV compared to pure TiO<sub>2</sub> (3.2 eV), and the doping was accompanied by a higher rate of recombination of photogenerated electron–hole pairs. A heterostructure was fabricated between the modified titania and g-C<sub>3</sub>N<sub>4</sub> to efficiently separate the carriers. An easy and cost-effective sol–gel process followed by a co-calcination technique was used to synthesize the nanostructured composite. The optimum dopant concentration and the extent of doping were investigated *via* XRD, Raman, XPS, TEM, and PL analyses, followed by a photocatalytic study. The impact of the band positions was investigated *via* UV-DRS and EIS. The dynamic nature of the band alignment at the depletion region of the heterojunction increased the carrier mobility from the bulk to active sites. The photogenerated electrons and holes retained their characteristic redox abilities to generate both OH<sup>•</sup> and O<sub>2</sub><sup>•-</sup> through a z-scheme mechanism. The photocatalytic activity resulted in superior photocatalytic H<sub>2</sub> evolution along with the defragmentation of bromoxynil, a persistent herbicide. The active catalyst exhibited 97% degradation efficiency towards pollutants along with 0.86% apparent quantum efficiency during the H<sub>2</sub> evolution reaction.

Received 21st June 2021  
Accepted 8th September 2021

DOI: 10.1039/d1na00460c

rsc.li/nanoscale-advances

## 1. Introduction

In recent years, there has been great interest in advanced photocatalytic technology because it can be applied to environmental and energy-harnessing projects.<sup>1–3</sup> A versatile and green photocatalyst for these projects could be developed with the assistance of different semiconducting materials.<sup>4</sup> A breakthrough in evergreen technology resulted in expansion of the field by the development of numerous semiconductor-based photocatalysts.

Among all the photocatalysts scrutinized to date, TiO<sub>2</sub> is the most promising candidate due to its outstanding characteristics, including its optical and electronic properties as well as its low cost, nontoxicity, high stability, and strong oxidizing capacity. Unfortunately, the optoelectronic phenomenon of TiO<sub>2</sub> is significantly hampered due to its wide band gap and excessive recombination rate of photo-excited electron–hole pairs.<sup>5,6</sup> Because of this considerable disadvantage, TiO<sub>2</sub> is

inoperative under visible light, and its applications are limited in many areas.

To overcome these problems, diversification has been performed to modify its band gap and strengthen its visible light photocatalytic activity through doping.<sup>6–8</sup> Metal modification and metal/nonmetal doping processes are advantageous because the physical characteristics and the electronic architecture of semiconducting materials can be altered to fit a wide variety of practical applications. However, this type of strategy can sometimes induce a defect level, which enhances the visible light absorption ability by reducing the energy threshold, where the defect level acts as a recombination zone for photo-induced carriers.

It is noteworthy that this particular issue can quench photocatalytic efficiency.<sup>9</sup> Therefore, ideas for reliable nanocomposites and heterostructures have been developed, including an upgrade for the photocatalytic performance of doped TiO<sub>2</sub> by decorating an appropriate semiconducting material with a precise band gap to construct suitable heterojunctions.<sup>10–12</sup> The heterojunctions effectively separate the photogenerated electron and hole (e<sup>-</sup>–h<sup>+</sup>) pairs, and also assist in the transportation of the charge carriers to the active site of the reaction.<sup>13</sup>

Department of Chemistry, National Institute of Technology, Rourkela, Odisha, India.  
E-mail: rkpahel@nitrkl.ac.in; souman27@gmail.com; Fax: +91-0661-246-2651; Tel: +91-0661-246-2652; +91-9437245438

† Electronic supplementary information (ESI) available. See DOI: 10.1039/d1na00460c



Graphene carbonitrides ( $g\text{-C}_3\text{N}_4$ ) have been used to improve the photocatalytic performance of  $\text{TiO}_2$ <sup>14</sup> because  $g\text{-C}_3\text{N}_4$  is a novel metal-free polymeric semiconductor with a narrow band gap (2.6–2.8 eV) that can be smoothly irradiated by visible light. It has a high surface area, more optimal conductivity, and an exceptional layered structure similar to that of graphene.<sup>15–17</sup>  $g\text{-C}_3\text{N}_4$  is a sustainable, cost-effective, environmentally friendly, and visible light-sensitive semiconductor that can be synthesized by a one-pot thermolysis procedure. The photocatalytic performance of pure  $g\text{-C}_3\text{N}_4$  is comparatively negligible due to the high recombination movement of promoted photo-excited carriers. However, the separate components of the  $g\text{-C}_3\text{N}_4/\text{TiO}_2$  nanocomposite work synergistically with excellent performance in the active oxidation process (AOP) by diminished  $e^- - h^+$  recombination with improved carrier mobility.<sup>18,19</sup>

The intimate heterostructure should have a suitable band edge of the valence band (VB) and conduction band (CB) for both semiconductors, which would create a depletion region involved in overall conductivity and activity of the material, depending on the types of contacts.<sup>20</sup> Several heterostructures can be fabricated using  $g\text{-C}_3\text{N}_4$  as the parent material, such as template-free mesoporous  $g\text{-C}_3\text{N}_4@\text{TiO}_2$  described by Hao *et al.*, for pollutant mineralization under visible light.<sup>21</sup> Zhang *et al.* prepared self-assembled cotton-fabricated  $g\text{-C}_3\text{N}_4/\text{TiO}_2$  and investigated its catalytic activity.<sup>19</sup> Other z-scheme photocatalysts such as  $\text{Ag}_2\text{CO}_3/\text{Ag}/\text{WO}_3$ ,  $\text{TiO}_2/g\text{-C}_3\text{N}_4-(\text{IO}_3^-/\text{I}^-)$ ,  $\text{CdS}/\text{rGO}/g\text{-C}_3\text{N}_4$ ,  $\text{Bi}_2\text{MoO}_6/\text{CNTs}/g\text{-C}_3\text{N}_4$ ,  $\text{SrTiO}_3:\text{La}$ , and  $\text{Rh}/\text{Au}/\text{BiVO}_4$  have also been adapted.<sup>22–26</sup> These z-scheme combinations are noble metal-based or a combination of redox pair catalysts that lead to higher cost and lower stability. In addition, the use of a high band-gap material drastically diminishes the light-harvesting ability, which subsequently minimizes the catalytic activity.

Because doping mainly relies on the ionic radii and coordination tendency of induced dopants, the selection of a dopant and determination of its optimum concentration will affect the resultant band structure of the material.<sup>27</sup> Herein, this work has mainly concentrated on tailoring the band position of  $\text{TiO}_2$  with the assistance of doping Zr at its lattice point by creating a donor level below the conduction band to enhance the light absorption efficiency towards the visible region. The optimum dopant concentration of Zr and the extent of lattice replacement were investigated with various characterizations, whereas nitrogen (N) was doped as a surface species ( $\text{NO}_x$ ) simply to increase the carrier conductivity.<sup>28</sup>

Because doping has its own drawbacks due to its action as a recombination zone, steps have been taken to establish a hetero-structure with  $g\text{-C}_3\text{N}_4$  because of its suitable band position with the doped system. The carrier transfers and separation efficiency within the junction of the heterostructure were determined by comparing the characterization and experimental outcomes, in which a z-scheme mechanism was confirmed. This z-scheme heterostructure was achieved using a binary system without any use of novel metals (as a mediator) or redox couples. Lastly, the heterojunction does well in terms of visible light absorption and carrier separation, which leads to photocatalytic  $\text{H}_2$  generation along with pollutant degradation.

## 2. Experimental section

### 2.1 Materials

Titanium tetraisopropoxide ( $\text{Ti}(\text{OCH}(\text{CH}_3)_2)_4$ ), urea,  $\text{ZrOCl}_2$ , ethanol,  $\text{HCl}$ ,  $\text{NH}_4\text{OH}$ , methanol, and indium tin oxide (ITO) glass were purchased from Sigma-Aldrich Chemicals, India. Isopropanol, *p*-benzoquinone (BQ), ethylenediaminetetraacetic acid disodium salt (2Na-EDTA), rhodamine B (Rh B), nitroblue tetrazolium (NBT), terephthalic acid (TA), and bromoxynil were acquired from Hi Media Chemicals, India. All chemicals were of analytical grade and used without further purification.

### 2.2 Synthesis of zirconium and nitrogen co-doped $\text{TiO}_2/g\text{-C}_3\text{N}_4$

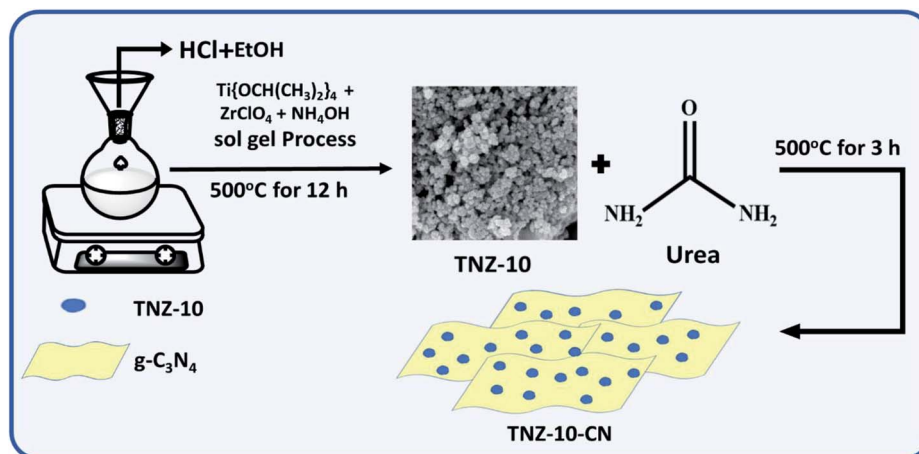
A series of zirconium and nitrogen co-doped titania (TNZ-*x*) were synthesized by the sol-gel technique. To a solution of 5 mL deionized water and 35 mL ethanol, a certain amount of  $\text{ZrOCl}_2$  was added with continuous stirring for 30 min at room temperature. Then, 12 mL of titanium isopropoxide and 3 mL of concentrated  $\text{HCl}$  were added, followed by the subsequent addition of 3 mL of 25% ammonium hydroxide solution (N precursor). The white gel formed remained undisturbed for 24 h. After that, it was dried at 100 °C for 12 h followed by calcination at 500 °C for 12 h. A series of materials was synthesized by maintaining a constant N dopant concentration and varying the percentage, where  $x$  (wt%) =  $(\text{Zr}/(\text{Zr} + \text{Ti}))$ . The zirconium and nitrogen co-doped titania material is abbreviated as TNZ-10, TNZ-20, and TNZ-30 where *x* denotes 10, 20, and 30 wt% of  $\text{ZrOCl}_2$ , respectively. Again, for comparison purposes, pure  $\text{TiO}_2$  was synthesized by the above process without the addition of  $\text{ZrOCl}_2$  and  $\text{NH}_4\text{OH}$  solution.

The heterostructured composite of zirconium and nitrogen-doped  $\text{TiO}_2/g\text{-C}_3\text{N}_4$  was synthesized by a simple one-pot solid-state annihilation method using urea as a precursor for graphene carbon nitride (CN). TNZ-*x*% at different weight ratios and urea (1 : 2, 1 : 4, and 1 : 6) were ground to a fine powder and subsequently calcined at 500 °C for 3 h with a ramp rate of 5 °C per min. The overall synthetic procedure is shown in Scheme 1. Out of all combinations, the 1 : 4 ratios of TNZ-10 and urea (abbreviated as TNZ-10-CN) exhibited the most optimal possible catalytic activity and were chosen for further study. The corresponding results are presented in the ESI Table T1.†

### 2.3 Instrumentation and measurements

The preliminary results regarding the crystalline phase of nanoparticles (NPs) were obtained from an X-ray diffraction study using a Philips PW 1830 X-ray diffractometer with a  $\text{Cu-K}\alpha$  radiation source. For the morphological analysis, transmission electron microscopy (TEM) and high-resolution transmission electron microscopy (HRTEM) were performed, and selected area electron diffraction (SAED) patterns were obtained using a Tecnai G2 F20 electron microscope with a voltage of 200 kV.

The X-ray photoelectron spectroscopy (XPS) was recorded on a PHI 5000 Versa Probe-III. The Fourier transform infrared (FTIR) spectra (400–4000  $\text{cm}^{-1}$  range) of as-prepared materials were recorded using a KBr disc with a RX-I FTIR



Scheme 1 A schematic representation of the synthetic approach used to produce the TNZ-x(wt%)-CN photocatalyst.

spectrophotometer (PerkinElmer USA). The UV-Vis absorption and reflectance spectra in solutions ( $\text{H}_2\text{O}$ ) as well as solids (diffuse reflectance spectroscopy, DRS) were obtained using a UV-Vis spectrophotometer (UV-2450 PerkinElmer). The photoluminescence (PL) emission spectra of photocatalysts in solid and also in solution phase were measured by a Fluoromax 4P spectrophotometer (Horiba Jobin Yvon USA) at an excitation wavelength of 345 nm. The electrochemical impedance analysis and the Mott-Schottky plots were carried out by using cyclic voltammetry (CV) with an AUTOLAB 302N modular potentiostat.

#### 2.4 Photocatalytic degradation study

The catalytic degradation efficiency was studied by choosing bromoxynil (a widely used herbicide) and rhodamine B dye as model pollutants for a scavenger and reactive species quantification study. In detail, 50 mg of the prepared photocatalyst was dispersed in 50 mL of a  $20 \text{ mg L}^{-1}$  organic pollutant solution. The catalytic performance was tested under a visible light source simulator (Lelesil quartz photo chamber with 250 W xenon light source and 420 nm cut-off filter).

Before irradiation of the light source, the solution was stirred in the dark for 60 minutes to achieve adsorption-desorption equilibrium. The solution was then irradiated under a visible light source, and thereafter, every 15 minutes, a 5 mL aliquot was removed and centrifuged to separate the catalyst. Then, the supernatant was analyzed by UV-Vis spectrophotometer and HPLC to determine the remaining pollutant concentration in it. The photocatalytic study revealed that the composite TNZ-10-CN had shown the highest pollutant breakdown activity.

#### 2.5 Photocatalytic $\text{H}_2$ evolution experiments

The hydrogen evolution experiment was carried out in a gas-closed circulatory apparatus. A 100 mg sample was dispersed in 100 mL of a solution of 80 mL of  $\text{H}_2\text{O}$  and 20 mL methanol as a sacrificial agent. The temperature of the system was maintained at a constant  $20^\circ\text{C}$ . A 250 W xenon lamp was used as a light source with a cut-off filter ( $\lambda > 420 \text{ nm}$ ), and the power

density was set to  $100 \text{ mW cm}^{-2}$  before each test. The quantity of evolved  $\text{H}_2$  was analyzed by an online gas chromatograph (GC-7920) equipped with a thermal conductivity detector.

#### 2.6 Quantification of reactive species and scavengers

For the trapping of reactive species such as hydroxide radicals ( $\text{OH}^\cdot$ ), superoxide radicals ( $\text{O}_2^{\cdot-}$ ), and holes ( $\text{h}^+$ ) involved in the active photocatalytic process, 1 mM IPA ( $\text{OH}^\cdot$  quencher), 1 mM BQ ( $\text{O}_2^{\cdot-}$  quencher), or 1 mM 2Na·EDTA ( $\text{h}^+$  quencher) was added to the pollutant. A similar method was followed for the quantitative analysis of  $\text{O}_2^{\cdot-}$  by conducting the nitroblue tetrazolium (NBT) test,<sup>29</sup> where the sample was added to  $2.5 \times 10^{-5}$  mole per L NBT solution, and the concentration of NBT at different time intervals was observed by UV-Vis spectrophotometer (absorption maximum at 259 nm). The above study was similar to that of the photocatalytic activity test except that the pollutants were replaced with an NBT solution. Terephthalic acid (TA) was used as a probe to quantify the amount of  $\text{OH}^\cdot$  radicals generated during the photocatalytic study. In brief, 0.1 g of the catalyst was dispersed in a 100 mL aqueous solution of TA ( $5 \times 10^{-4} \text{ mol L}^{-1}$ ) and NaOH ( $2 \times 10^{-3} \text{ mol L}^{-1}$ ) at room temperature. The suspension was irradiated by visible light. TA reacts with  $\text{OH}^\cdot$  radicals to produce 2-hydroxyterephthalic acid, which is a highly fluorescent product (fluorescence peak at 425 nm and excitation wavelength of 315 nm).<sup>30</sup>

#### 2.7 Electrochemical impedance spectroscopy (EIS)

EIS analysis was conducted using an AUTOLAB 302N modular potentiostat based upon a three-way electrode system that includes a platinum wire as a counter electrode, Ag/AgCl as the reference electrode, and a working electrode, which was fabricated on indium tin oxide (ITO) glass. Typically, 5 mg of the prepared sample was added to 0.5 mL dimethylformamide, and a dense slurry was created by sonication for several minutes. The slurry was evenly dispersed on an exposed area  $1 \text{ cm}^2$  in size and dried at  $80^\circ\text{C}$  in a hot-air oven. Then, it was heated at  $200^\circ\text{C}$  for 1 h for greater adhesion. The electrolyte used was a 0.1 M  $\text{Na}_2\text{SO}_4$  aqueous solution without other additives.

### 3. Results and discussion

#### 3.1 XRD analysis

The extent of crystallinity and phase of the nanocomposite was studied using an X-ray diffraction technique. Fig. 1a exhibits the XRD data for the composites and root materials formed. The typical peaks observed at 25.15°, 37.38°, 47.78°, 53.34°, 54.75°, 62.19°, and 74.39° correspond to the (101), (004), (200), (105), (211), (204), and (125) crystal planes of the anatase phase of titania (JCPDS 21-2172), respectively.<sup>31</sup> A small satellite peak (star marked), observed at 27.21°, is due to the presence of g-C<sub>3</sub>N<sub>4</sub> and represents the (002) plane, but the insignificant peak intensity is due to the low crystallinity of g-C<sub>3</sub>N<sub>4</sub> in comparison to titania.<sup>32,33</sup> The origination of the (002) plane is due to the interlayer reflection of the graphite-like structure. The sharp rise in a peak at 30.58°, regarding crystal plane (111), is due to the enhanced doping of zirconium (Fig. S1a†). It was observed that Zr doping at 10 wt% did not have any effect on the XRD pattern, but with further increase in doping, the peak at 30.58° increased, and at approximately 40% dopant concentration, the phase was completely changed (Fig. S1a†).

Upon doping of nitrogen, there is no net change in the lattice parameters of samples TiO<sub>2</sub> and N-TiO<sub>2</sub>, and therefore, the presence of nitrogen at the lattice is not a valid consideration.

Therefore, nitrogen could exist as a surface species as (NO)<sub>x</sub>, which would enhance the carrier mobility over the surface.<sup>28</sup> The enlarged (101) XRD peak of samples is displayed in Fig. S1b.† No peak shift was observed in the case of the N-doped and undoped system, whereas the peaks of TNZ-10, TNZ-15, and TNZ-30 shift to a lower diffraction angle as the Zr concentration is increased (Fig. S1b†). From the above considerations, the presence of Zr at the lattice point of titania can be predicted by the positive change in lattice parameters and shifting of the peak to a lower diffraction angle.<sup>28</sup>

#### 3.2 Raman analysis

The characteristic vibrational stretching bands observed at 144, 197, 396, 516, and 640 cm<sup>-1</sup> correspond to the E<sub>g</sub>, B<sub>1g</sub>, A<sub>1g</sub>, B<sub>1g</sub>, and E<sub>g</sub> modes of the anatase phase of titania (Fig. 1b), respectively.<sup>34</sup> As the percentage of zirconia is enhanced, a new satellite peak at 280 cm<sup>-1</sup> is observed in TNZ-15 and TNZ-30, but no changes are observed for TNZ-10. A newly formed satellite peak at 280 cm<sup>-1</sup> is observed as a vibrational mode of the ZrTiO<sub>3</sub> phase. In Zr-doped systems, the peak at 144 cm<sup>-1</sup> shifts to a lower wavenumber, with an increase in dopant concentration, and the shifting is more frequent as concentration increases. In contrast, no shifting in the 144 cm<sup>-1</sup> peak was observed when a comparison was performed between Zr, N-doped titania, and the Zr-

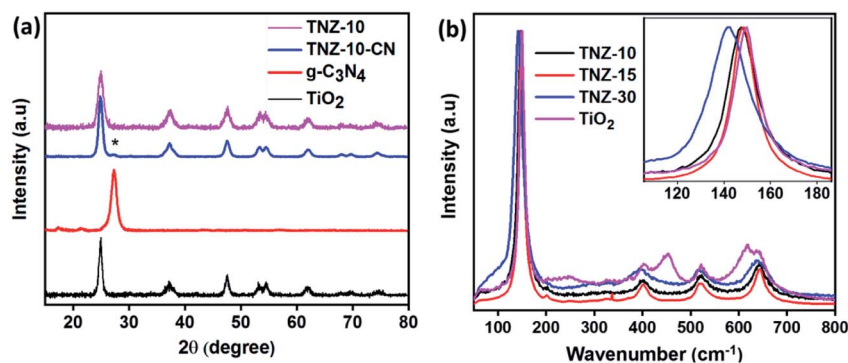


Fig. 1 (a) The XRD patterns of g-C<sub>3</sub>N<sub>4</sub>, TiO<sub>2</sub>, Zr- and N-doped titania (TNZ-10), and its composite. (b) Raman spectra of pure TiO<sub>2</sub> and 10, 20, and 30% Zr-doped TiO<sub>2</sub>.

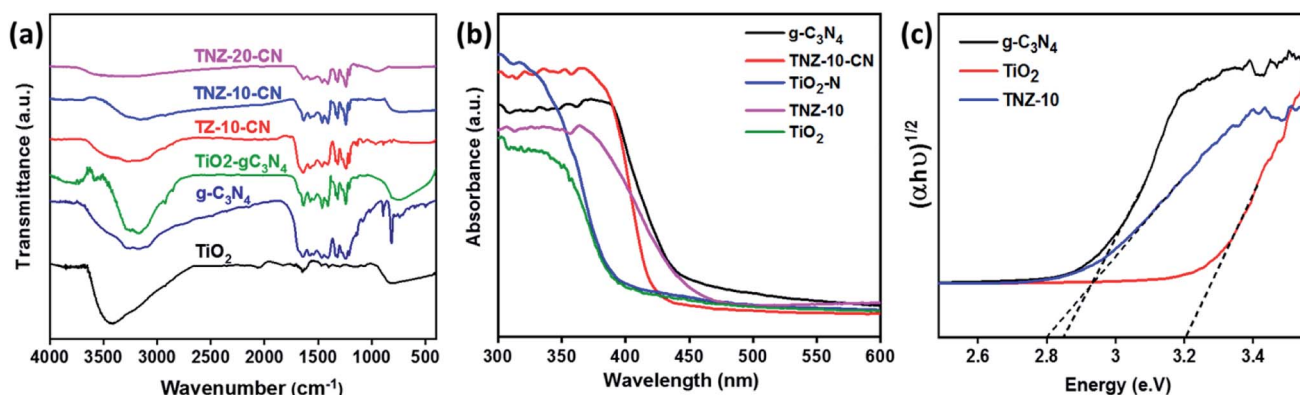


Fig. 2 (a) FTIR spectra of g-C<sub>3</sub>N<sub>4</sub>, TiO<sub>2</sub>, and different doped composites. (b) UV-vis DRS spectra of the parent constituents and different composites. (c)  $(\alpha h\nu)^{1/2}$  vs.  $h\nu$  plots showing the corresponding band gaps.



doped system (Fig. S2†). Therefore, it could be concluded that Zr ion (72 pm) substitution occurred at the lattice point of Ti (53 pm), which can be further explained by the equation below.<sup>28</sup>

$$\bar{\nu} = \frac{1}{2\pi c} \sqrt{\frac{k}{\mu}} \quad (1)$$

where  $\bar{\nu}$  = wave number ( $\text{cm}^{-1}$ ),  $\mu$  = reduced mass of bound elements,  $k$  = force constant (bond strength), and  $c$  = velocity of light. The stretching of Zr–O is less as compared to Ti–O interaction due to the larger size of  $\text{Zr}^{4+}$  with respect to  $\text{Ti}^{4+}$ . As per the results, stress is induced by the substantial replacement of Ti by Zr in the lattice point, which results in a decrease in the vibrational frequency of the  $E_g$  band.<sup>35</sup> The Raman spectra provide satisfactory agreement with the XRD data towards the doping theory.

### 3.3 FTIR analysis

Fig. 2a reveals the FTIR spectra and the nature of the interaction between the elements of the parent constituents and hybrid

composites  $g\text{-C}_3\text{N}_4$ , TNZ-10, and TNZ-10-CN. An absorption band is observed in the range of  $500\text{--}800\text{ cm}^{-1}$  due to the stretching vibration of Ti–O–Ti. The fine peak at  $802\text{ cm}^{-1}$  is assigned to the out-of-plane breathing vibration of the *s*-triazine units.<sup>36</sup> The band of peaks between  $1300$  and  $1700\text{ cm}^{-1}$  is due to the various stretching modes between C=N and C–N of heptazine-derived repeating units.<sup>37</sup> A broad band obtained from  $3000\text{--}3600\text{ cm}^{-1}$  is ascribed to vibrational stretching modes of the N–H groups of  $g\text{-C}_3\text{N}_4$ .

### 3.4 Optical characterization

UV-visible diffuse reflectance spectra were obtained to illustrate the band structure and optical absorption property of the materials (Fig. 2b and c). The bandgap can be derived from the Kubelka–Munk function:<sup>38</sup>

$$(\alpha h\nu)^{\frac{1}{2}} = (A h\nu - E_g) \quad (2)$$

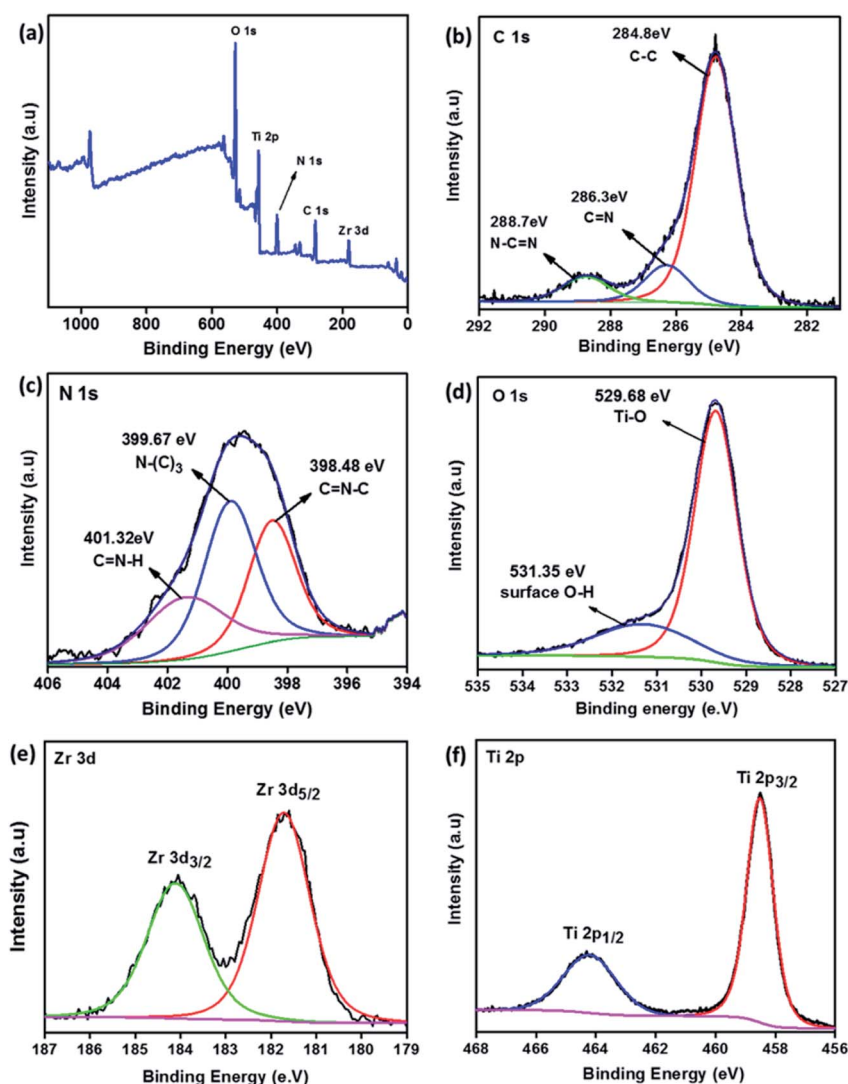


Fig. 3 XPS spectra. (a) The survey spectrum of the composite TNZ-10-CN. High-resolution spectra of constituent elements: (b) C 1s, (c) N 1s, (d) O 1s, (e) Zr 3d, and (f) Ti 2p.

where,  $\alpha$ ,  $A$ ,  $h\nu$ , and  $E_g$  denote the absorption coefficient, a constant, photo energy, and band gap, respectively (eqn (2)). The band gap of  $\text{TiO}_2$  is approximately 3.20 eV because the band threshold is centered at 402.6 nm. The optical absorbance of  $\text{TiO}_2\text{-N}$  did not shift compared to pure  $\text{TiO}_2$ , and this indicates that the presence of N as a surface  $\text{NO}_x$  species cannot alter the band edge. Similarly, the absorption edge of  $g\text{-C}_3\text{N}_4$  is located at 456.7 nm with a band gap of 2.84 eV. The band gap of TNZ-10 is 2.8 eV with an absorption wavelength of 456.2 nm, which shows a redshift in absorption in comparison to pure  $\text{TiO}_2$ . For the TNZ-10 with a 10% dopant concentration, a defect energy level is created below the CB, which results in strong absorption of photons in the visible region because of the electron transition from VB to the  $\text{Zr}^{4+}$  defect level.<sup>39</sup> As a result, the exact band edge of the pristine  $\text{TiO}_2$  is altered. The precise band edge of the doped and undoped system has been studied from Mott-Schottky plots. The final composite TNZ-10-CN heterostructure led to the generation of additional excitons under visible light irradiation because the band threshold is between its constituents.

### 3.5 XPS analysis

The surface chemical composition and elemental state of individuals in the composite were studied by XPS. Fig. 3a shows

the survey spectrum of composite TNZ-10-CN, which consists of C, N, O, Ti, and Zr. Fig. 3b-f illustrates the high-resolution XPS spectra of the corresponding C 1s, N 1s, O 1s, Ti 2p, and Zr 3d. The deconvoluted high-resolution XPS spectra of C 1s (Fig. 3b) show three peaks at 284.8 eV, 286.3 eV, and 288.7 eV. The peak at 284.8 eV corresponds to the  $\text{sp}^2$  hybridized C-C bond in  $g\text{-C}_3\text{N}_4$  (CN). The peak at 286.3 eV is attributed to the C=N groups, and the peak centered at 288.7 eV is due to the  $\text{sp}^2$  hybridized C (N-C=N) in  $g\text{-C}_3\text{N}_4$ .<sup>40,41</sup> In the N 1s spectra (Fig. 3c), the peak at 398.44 eV is attributed to the  $\text{sp}^2$  hybridized aromatic C-N=C group. The peak at 398.94 eV is derived from tertiary N-(C)<sub>3</sub> of the triazine CN unit, whereas the 400.05 eV peak is due to the C-N-H unit. The high-resolution O 1s curve (Fig. 3d) of the composite TNZ-10-CN is fitted into two peaks, whereby the peak at 529.68 eV is attributed to the Ti-O bond in the  $\text{TiO}_2$  lattice, and the peak at 531.35 eV is ascribed to the O-H bond. The Ti 2p spectrum (Fig. 3f) is fitted to two peaks, 464.23 eV and 458.51 eV, which are ascribed to the Ti 2p<sub>1/2</sub> and Ti 2p<sub>3/2</sub> spin-orbit peaks of  $\text{TiO}_2$ , respectively.<sup>42</sup> The deconvoluted high-resolution XPS peak centered at 181.73 eV is due to the Zr 3d<sub>5/2</sub> spin-orbit peak of the substitutionally inserted  $\text{Zr}^{4+}$  ion (Fig. 3e). This peak falls between metallic Zr (179.0 eV) and the Zr 3d<sub>5/2</sub> peak of  $\text{ZrO}_2$  (183.5 eV), and therefore, it can be concluded that the  $\text{Zr}^{4+}$  ions were substituted into the lattice of

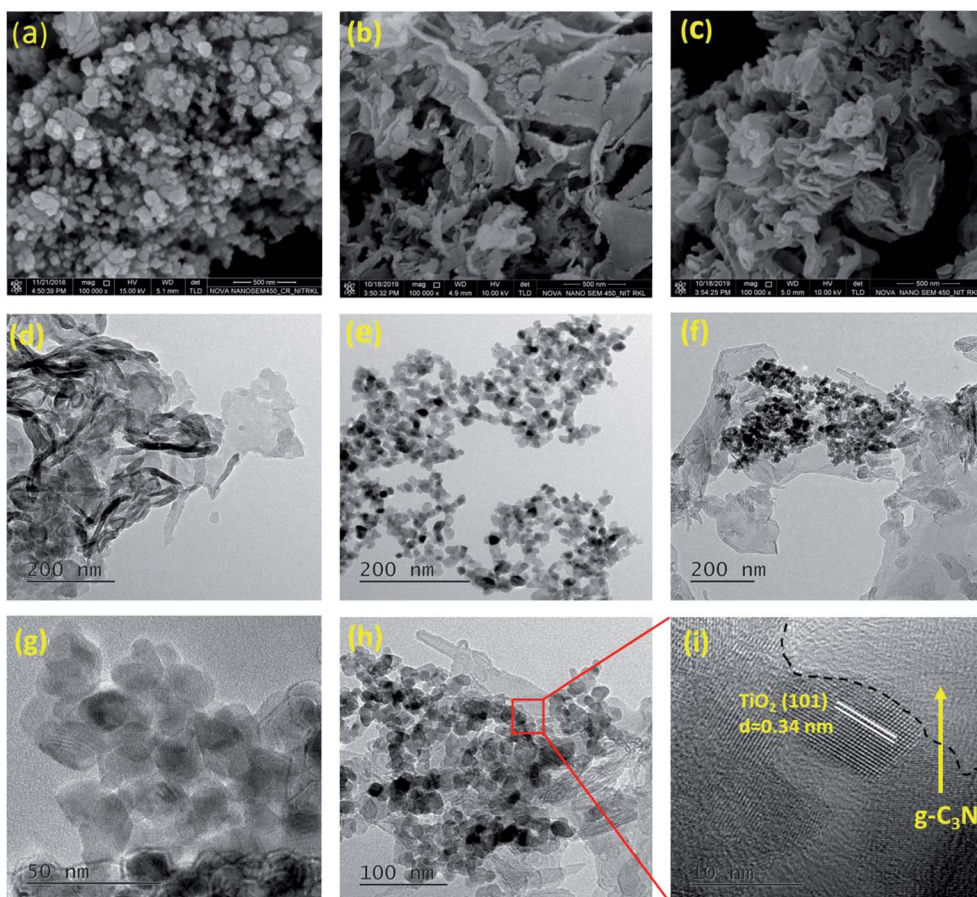


Fig. 4 FE-SEM images of (a) TNZ-10, (b)  $g\text{-C}_3\text{N}_4$ , and (c) TNZ-10-CN. TEM images of (d)  $g\text{-C}_3\text{N}_4$ , (e) TNZ-10, and (f) TNZ-10-CN; and magnified images of (g) TNZ-10 and (h) TNZ-10-CN. (i) A HR-TEM image of TNZ-10-CN.

TiO<sub>2</sub> by replacing Ti<sup>4+</sup> ions, with an increase in dopant concentration, which justifies the observations of XRD and Raman spectroscopy.<sup>43</sup>

### 3.6 Morphological analysis

The structure and particle size of TNZ-10-CN and its reference samples were investigated by FESEM, TEM, and HR-TEM analysis (Fig. 4). TNZ-10 (Fig. 4a) is mainly composed of nanoparticles with a size range of 10–30 nm, whereas g-C<sub>3</sub>N<sub>4</sub> has a sheet-like structure (Fig. 4b), but the decoration of TNZ-10 over the g-C<sub>3</sub>N<sub>4</sub> nanosheet is not well documented from FESEM images (Fig. 4c). Therefore, TEM was performed to view the nanosheet with a higher rate of magnification. Fig. 4d–f displays the TEM image of g-C<sub>3</sub>N<sub>4</sub>, TNZ-10, and TNZ-10-CN, respectively. The TEM images show that the TNZ-10 nanoparticles are well-dispersed over the nanosheet, and the intimate contact between the nanoparticles with g-C<sub>3</sub>N<sub>4</sub> results in heterojunctions that lead to high conductivity and charge separation efficiency.<sup>44</sup> The HRTEM image of TNZ-10-CN and TNZ-10 depicts the distinct lattice fringes of TiO<sub>2</sub> with a *d*-spacing of 0.34 nm corresponding to the TiO<sub>2</sub> (101) planes.<sup>45</sup>

The SAED pattern of g-C<sub>3</sub>N<sub>4</sub> shows amorphous architecture, whereas TNZ-10 is polycrystalline with more prominent rings. The heterostructure of TNZ-10-CN exhibits a mixed character, as the pattern is more defused in comparison to TNZ-10 (Fig. S3a–c†). Furthermore, EDS mapping of TNZ-10-CN was performed for the confirmation of elemental composition (Ti, Zr, O, C, N) and their distribution throughout the composite (Fig. S3d–i†). Additionally, the EDAX study of the TNZ-10-CN heterostructure validated the presence of C, N, Ti, Zr, and O elements (Fig. S4†). The above results match the results from XRD as well as XPS. Both parent compounds make intimate contact, which significantly enhances the charge separation during the photo-catalytic oxidation process. The overall morphological analysis demonstrates that the TNZ-10-CN photocatalyst was successfully fabricated by a simple co-calcination process.

### 3.7 Surface area and pore size distribution

The N<sub>2</sub> adsorption-desorption isotherms were obtained to investigate the pore size distribution and the corresponding specific surface area of the prepared sample (Fig. 5). All the

samples exhibit isotherm IV with a type H3 hysteresis loop, illustrating that the sample g-C<sub>3</sub>N<sub>4</sub>, TNZ-10, and the composite TNZ-10-CN possess a mesoporous structure, which can also be established from the pore size distribution plot (Fig. 5b). The hysteresis loop displays an intra-aggregated pore distribution at low partial pressure ( $0.4 < P/P_0 < 0.8$ ), and at a higher partial pressure value, large pores stacked between secondary particles were observed. All samples displayed a pattern of bimodal pore distribution with a primary contribution in the range of 2–4 nm and a secondary contribution in a 8–12 nm range. The BET surface area of TNZ-10-CN was found to be 49.8 m<sup>2</sup> g<sup>-1</sup>, which is higher than that of the individual constituents (g-C<sub>3</sub>N<sub>4</sub> 10.65 m<sup>2</sup> g<sup>-1</sup> and TNZ-10 8.03 m<sup>2</sup> g<sup>-1</sup>). The apparent increase in the surface area provides more optimal catalytic active sites, which results in increased photocatalytic performance.

### 3.8 Photoluminescence performance

To determine the efficient migration and separation of photo-generated electron-hole pairs, photoluminescence (PL) analysis was conducted for TNZ-10, g-C<sub>3</sub>N<sub>4</sub>, and TNZ-10-CN (Fig. 6a). The intensity of the PL spectra primarily depends on the photo-generated electron-hole recombination rate. The lower the PL spectra intensity, the higher the separation efficiency.<sup>46</sup> The emission peak centered at 455 nm corresponds to g-C<sub>3</sub>N<sub>4</sub> with a narrow band gap of 2.85 eV, which indicates a higher carrier recombination rate. However, the TNZ-10-CN heterostructure shows a massive drop in emission intensity, which suggests greater separation and migration of electron-hole pairs, although the high band gap for TNZ-10 barely shows any emission peak in the range of 350–650 nm.<sup>47</sup>

### 3.9 Electrochemical impedance analysis (EIS)

EIS analysis (Nyquist plot) was performed to measure the extent of charge carrier migration and separation efficiency of photo-generated electron-hole couples. The graph displays a high-frequency semicircle section with a different arc radius. Evidently, the arc radius of the TNZ-10-CN composite as a working electrode is the lowest in comparison to that of its root materials. This indicates higher charge mobility and lower interfacial resistance of the composite (Fig. 6b), which implies a lower rate of recombination of excitons.<sup>48</sup> A comparison of the

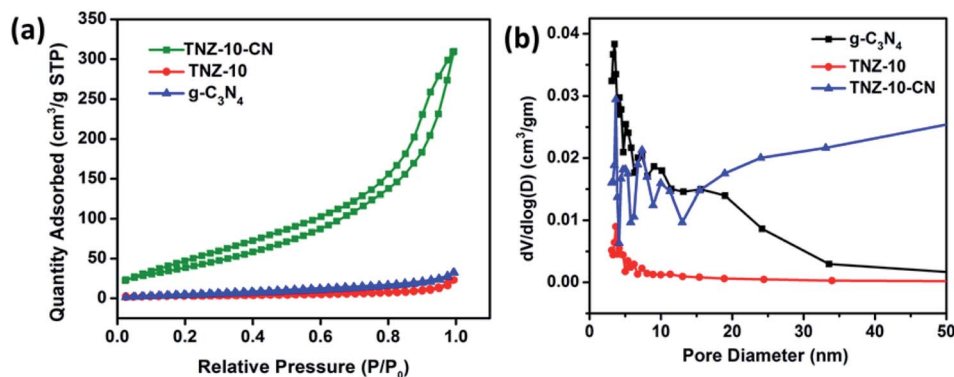


Fig. 5 (a) Nitrogen physisorption isotherms and (b) pore size distributions calculated via the Barrett–Joyner–Halenda (BJH) method.



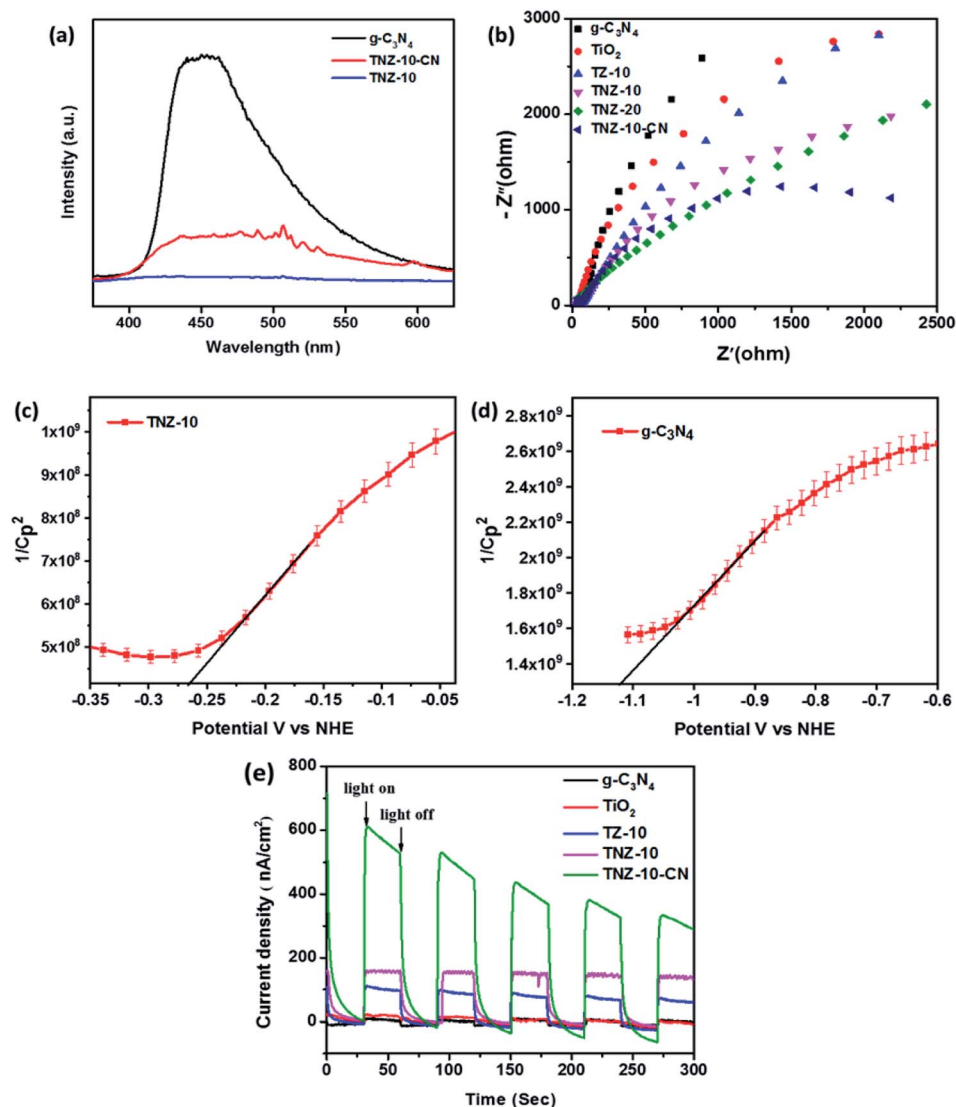


Fig. 6 (a) PL spectra of pure  $g-C_3N_4$ , TNZ-10, and TNZ-10-CN. (b) EIS Nyquist plots, Mott-Schottky plots of (c) TNZ-10 and (d)  $g-C_3N_4$ , and (e) the photocurrent responses of the heterojunctions.

EIS plots of TNZ-10 and TNZ-10 reveals less resistance towards carrier mobility for the latter, as it has a smaller arc radius in comparison to the former, which explains how the presence of N, which is considered as a surface species, strengthens the separation efficiency. However, the position of N is at the surface and not in a lattice space, which has already been elucidated in the XRD and Raman analysis. The Mott-Schottky analysis was also carried out to determine the flat band position, as well as the type of semiconductor-based parent materials. The impedance studies were performed in the dark, and the flat band potential ( $V_{fb}$ ) was measured using the following Mott-Schottky equation:<sup>49</sup>

$$\frac{1}{C_p^2} = \frac{2}{N_D \epsilon \epsilon_0 e A^2} \left( V - V_{fb} - \frac{kT}{e} \right) \quad (3)$$

where  $C_p^2$  = capacitance of depletion layer,  $T$  = absolute temperature (K),  $k$  = Boltzmann constant,  $e$  = charge of electron,  $V_{fb}$  = flat band potential,  $V$  = applied voltage,  $A$  = area in

$cm^{-2}$ ,  $N_D$  = donor density of states, and  $\epsilon$  and  $\epsilon_0$  are dielectric constants of semiconductor and vacuum respectively. Fig. 6c and d indicate that both root materials are n-type semiconductors, as per the positive slope in the Mott-Schottky plot. From the literature, it is well understood that the flat band potential of n-type semiconductors is roughly the same as the conduction band potential.<sup>50-52</sup> Thus, the conduction band (CB) of  $g-C_3N_4$  and TNZ-10 was examined and determined to be  $-1.12$  and  $-0.265$  V vs. normal hydrogen electrode (NHE), respectively, as per the intercept at the x-axis of the Mott-Schottky plot. Moreover, the transient photocurrent density technique was used to further justify the carrier separation and migration efficiency through the photocurrent response.

As mentioned in Fig. 6e, the TNZ-10-CN heterojunction shows a higher current density response, and manifests superior separation and migration of electron-hole pairs, which subsequently results in increased photocatalytic activity. The presence of N as a carrier mobilizer and its relative catalytic



activity can be summarised by comparing the TZ-10 and TNZ-10 samples, where the presence of N, embedded as a surface species, increases the photocurrent density and elucidates nitrogen's role in surface  $\text{NO}_x$  (Fig. 6e).  $\text{NO}_x$  also acts as an active catalytic site, and thus supports the overall redox process for the degradation of pollutants.

### 3.10 Photocatalytic activity and stability of TNZ-10-CN

A series of combinations was created by changing the dopant wt% and the weight ratio of the parent reference samples. The catalytic efficiency of the synthesized samples was evaluated by the degradation of bromoxynil (a very persistent herbicide) and Rh B, which was used as a probe pollutant for scavengers and the kinetics analysis. Fig. 7a and b shows that TNZ-10-CN exhibited the highest activity as compared to that of pure  $\text{g-C}_3\text{N}_4$ , TNZ-10, and their other combinations such as TNZ-20-CN and TNZ-30-CN (order: TNZ-10-CN > TNZ-20-CN >  $\text{TiO}_2@ \text{g-C}_3\text{N}_4$  > TNZ-30-CN > TNZ-10 >  $\text{g-C}_3\text{N}_4$ ). Pure  $\text{g-C}_3\text{N}_4$  displayed a very poor degradation efficiency of approximately 24% under visible light due to its high carrier recombination rate, whereas TNZ-10 exhibited 36% activity, which was concluded from UV-DRS and the PL analysis. The optimum dopant concentration (Zr) was found to be 10 wt% in comparison to its other hybrids. The degradation kinetics of different samples were simulated by pseudo-first order kinetics. The rate constant ( $k$ ) was calculated from eqn (4) given below:

$$\ln \frac{C_0}{C} = kt \quad (4)$$

where  $k$  denotes the rate constant in  $\text{min}^{-1}$ ,  $t$  denotes the reaction time,  $C_0$  denotes the initial concentration, and  $C$  denotes the concentration remaining at time  $t$ . The kinetics study of the degradation shown in Fig. 7b displays the poor catalytic activity of  $\text{g-C}_3\text{N}_4$  and TNZ-10. The  $k$  value of TNZ-10-CN is nearly 12 and 23 times higher than that of TNZ-10 and  $\text{g-C}_3\text{N}_4$ , respectively. The effect of the Zr-doped composite on Rh B mineralization exhibited a sequence: TNZ-10-CN > TNZ-20-CN > TNZ-30-CN, with respective  $k$  values of  $0.0512 \text{ min}^{-1}$ ,  $0.011 \text{ min}^{-1}$ , and  $0.0094 \text{ min}^{-1}$ .

A comparative study between the doped and undoped systems of the same parent materials was also performed. The 10 wt% Zr-doped composite (TNZ-10-CN) performed with 5 times superior catalytic activity as compared to undoped  $\text{TiO}_2@ \text{g-C}_3\text{N}_4$ . Furthermore, more optimal photocatalytic activity was observed for the TNZ-10-CN heterojunction in comparison to that of different  $\text{TiO}_2/\text{g-C}_3\text{N}_4$ -based photocatalysts (Table 1). As for the rate constant ( $k$  value), a  $k$  value of  $0.0512 \text{ min}^{-1}$  was measured for the composite TNZ-10-CN as compared to the  $k$  values for  $\text{TiO}_2@ \text{g-C}_3\text{N}_4$ , TNZ-20-CN, TNZ-10, and  $\text{g-C}_3\text{N}_4$ , which were  $0.010 \text{ min}^{-1}$ ,  $0.011 \text{ min}^{-1}$ ,  $0.007 \text{ min}^{-1}$ , and  $0.002 \text{ min}^{-1}$ , respectively (Fig. 7d). The stability and reusability of the TNZ-10-CN heterojunction was evaluated by conducting a catalytic cycle test using Rh B as a model pollutant. As shown in Fig. 7e, the catalyst displayed a lower photocatalytic

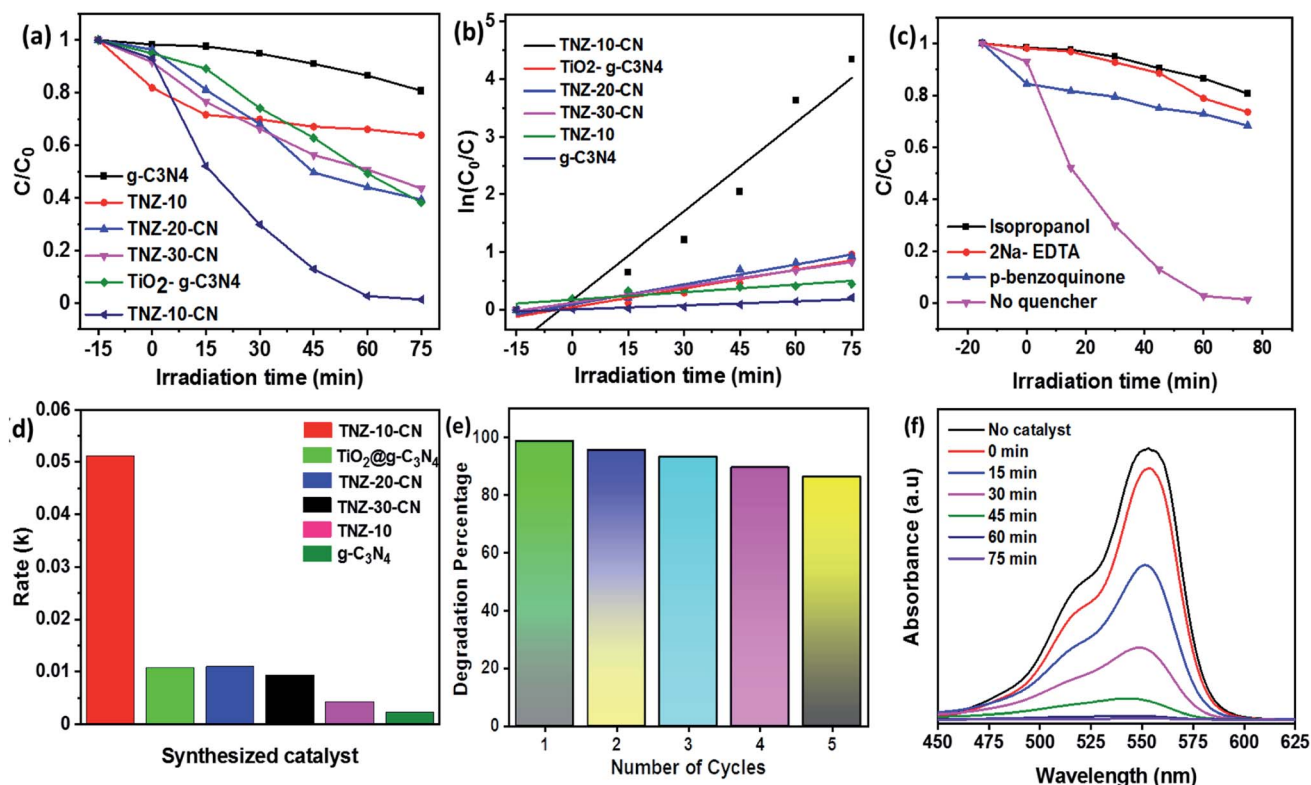


Fig. 7 (a) Photocatalytic degradation study of Rh B using the as-prepared samples, (b) respective kinetics data, (c) scavenger studies, (d) comparative rates of prepared samples, and (e) the catalyst cycling stability and (f) Rh B degradation at different times of TNZ-10-CN.

Table 1 A comparative study of TNZ-10–CN with other TiO<sub>2</sub>/g-C<sub>3</sub>N<sub>4</sub>-supported catalysts for dye degradation

Catalyst	$C_{\text{cat}}$ (mg mL <sup>-1</sup> )	$C_{\text{dye}}$ (mg L <sup>-1</sup> )	Source	Rate	Reference
g-C <sub>3</sub> N <sub>4</sub> /TiO <sub>2</sub>	1.0	Rh B, 10.0	500 W ( $\lambda > 420$ nm)	5.0 h, 84%	54
g-C <sub>3</sub> N <sub>4</sub> -P25	0.5	MB, 3.0	500 W ( $\lambda > 420$ nm)	5.0 h, 84%	55
g-C <sub>3</sub> N <sub>4</sub> /Ag/TiO <sub>2</sub>	1.0	MO, 13.5	300 W ( $\lambda > 420$ nm)	6.0 h, 100%	56
TiO <sub>2</sub> /g-C <sub>3</sub> N <sub>4</sub>	1.0	MO, 10.0	300 W ( $\lambda > 420$ nm)	90 min, 80%	57
g-C <sub>3</sub> N <sub>4</sub> /TiO <sub>2</sub>	1.0	Rh B, 10.0	300 W ( $\lambda > 420$ nm)	50 min, 96%	58
CNNC/TiO <sub>2</sub>	1.0	Rh B, 10.0	500 W ( $\lambda > 420$ nm)	60 min, 100%	59
TNZ-10–CN	1.0	Rh B, 20.0	250 W ( $\lambda > 420$ nm)	75 min, 98%	This work

performance of 82% after 5 catalytic cycles as compared to that of its first use.

The defragmentation of bromoxynil was investigated using an HPLC-UV chromatogram. Initially, a 20 ppm bromoxynil solution (without the treatment of catalyst and light) was analyzed *via* HPLC, and after that, samples withdrawn at 20 min time intervals were analyzed. Blank bromoxynil exhibited two peaks at 220 nm and 317 nm wavelength, and at 2.23 min of retention time. Over time, new peaks at different retention times were observed, and the intensities of characteristic peaks of bromoxynil were decreased (Fig. S6<sup>†</sup>). After 80 min of treatment, a single peak below 200 nm was witnessed. The peaks at different wavelengths with respect to the retention time and their corresponding area percentages are shown in Fig. S6<sup>†</sup>. The 3D degradation pattern of bromoxynil is shown in Fig. S5a–d,<sup>†</sup> from which a clear defragmentation pattern of bromoxynil can be observed. The degradation data of both pollutants indicates that the synthesized catalyst TNZ-10–CN functions properly in terms of light harvesting and satisfactorily with respect to carrier splitting capability.

The total organic carbon (TOC) experiment was very effective for estimating the mineralization rate of bromoxynil. Fig. 9d shows the removal percentage of organic carbon of the pollutant treated with the catalyst after 75 min of irradiation time. The catalyst TNZ-10–CN attained 76.2% removal in 75 min.

The higher degradation efficiency of TNZ-10–CN was achieved at moderate pH towards bromoxynil. This can be clarified by the conviction that when the pH is lower than the dissociation constant ( $pK_a = 4.1$ ), the phenolic form is the principal one

in the solution.<sup>53</sup> Furthermore, the zero point charge of TNZ-10–CN was calculated to be 4.19 (Fig. S7a<sup>†</sup>). Hence, the surface charge of the photocatalytic system was positive at  $\text{pH} < 4.19$ . When the pH was lower than the dissociation constant ( $pK_a = 4.1$ ), the protonated bromoxynil and the positively charged surface established an electrostatic force of repulsion, which diminished the degradation efficiency. However, at a higher pH, the enhanced performance is due to the force of attraction between bromoxynil and the surface of the material. The above consideration provides a more optimal surface interaction between catalyst and pollutant molecules at moderate pH, which leads to higher catalytic activity (Fig. S7b<sup>†</sup>).

### 3.11 Photocatalytic H<sub>2</sub> evolution performance and stability

The photocatalytic H<sub>2</sub> evolution of the active composite TNZ-10–CN has shown superior activity ( $147.32 \mu\text{mol h}^{-1}$ ) compared to that of various combinations of its root constituents (Fig. 8a). Different Z- and N-doped heterojunctions, such as TNZ-10–CN and TNZ-20–CN, displayed a subtle difference in terms of H<sub>2</sub> evolution activity, but beyond the optimum dopant (30 wt% of Zr) concentration, the H<sub>2</sub> evolution tendency drastically diminished. This occurred because over a certain limit, doping theory collapses by creating a new phase, which significantly affects the light-harvesting ability. Hence, doping in a system creates a donor energy level below the conduction band, which is able to tune the band structure.

This observation was verified by considering Zr- and N-doped TiO<sub>2</sub> (TNZ-10), Zr-doped TiO<sub>2</sub> (TZ-10), and TiO<sub>2</sub> and their respective H<sub>2</sub> evolution efficiencies ( $93.75 \mu\text{mol h}^{-1}$ ), ( $89.28 \mu\text{mol h}^{-1}$ ), and ( $87.05 \mu\text{mol h}^{-1}$ ). When blending the Zr-

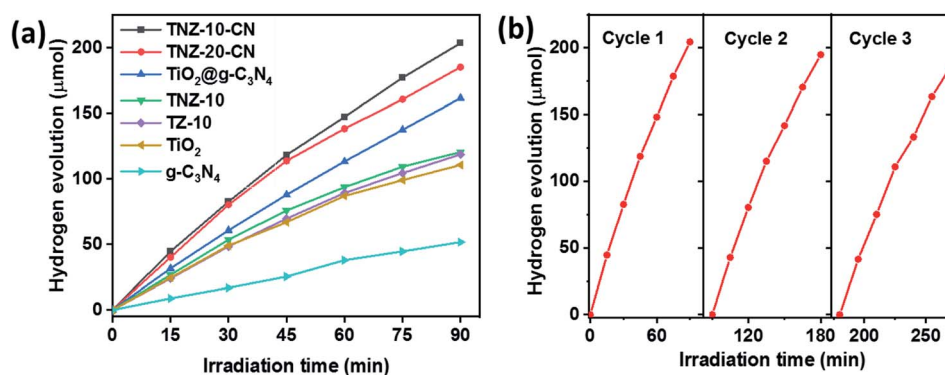


Fig. 8 (a) Time course of H<sub>2</sub> evolution per 100 mg of samples used. (b) Recycling efficiency testing of the photocatalyst TNZ-10–CN.

and N-doped  $\text{TiO}_2$  (TNZ) and  $g\text{-C}_3\text{N}_4$  (CN) to construct the heterojunction TNZ-10-CN (value 10 represents the dopant concentration), an  $\text{H}_2$  evolution efficiency of  $147.32 \mu\text{mol h}^{-1}$  was obtained, which is nearly 6 times higher than that of pristine  $g\text{-C}_3\text{N}_4$  and 2 times higher than that of pure  $\text{TiO}_2$ . However, the apparent quantum efficiency of the  $\text{H}_2$  conversion reaction increased to 0.86% (the detailed calculation is provided in the ESI†). This enhanced activity suggests that heterojunctions working synergistically will improve carrier separation and migration efficiency during overall photocatalytic activity, which was confirmed from PL and electrochemical impedance analyses. Moreover, the consistency of the photocatalyst plays an important role in predicting photocatalytic efficiency. As shown in Fig. 8b, the TNZ-10-CN sample exhibited a steady  $\text{H}_2$  evolution over three consecutive cycles for 3.5 h, without any appreciable deviation.

### 3.12 Photocatalytic mechanism

To comprehend the active oxygen process (AOP) mechanism of the TNZ-10-CN composite, the band edge alignments of individual constituents TNZ-10 and  $g\text{-C}_3\text{N}_4$  were analyzed from UV-DRS and Mott-Schottky plots. From the energy level diagram (Fig. 10), it is evident that the conduction band (CB) edge of  $g\text{-C}_3\text{N}_4$  is directly above the reduction potential of  $\text{O}_2/\text{O}_2^{\cdot-}$  ( $-0.33 \text{ V vs. NHE}$ ), while the CB potential of TNZ-10 is far below it. Thus, the band edge of  $g\text{-C}_3\text{N}_4$  has the ability to generate  $\text{O}_2^{\cdot-}$ . Similarly, the valence band (VB) edge of TNZ-10 is at a suitable position to produce  $\text{OH}^{\cdot}$ .

From the scavenger study and reactive species trapping experiment, the composite TNZ-10-CN exhibited higher activity

in terms of radical generation. The evidence of  $\text{OH}^{\cdot}$  generation was confirmed from the TA test. Fig. 9a shows that over time, the intensity of 2-hydroxy terephthalic acid (fluorescence wavelength at 425 nm) increases. From the comparative PL intensity graph (Fig. 9c), the heterostructure TNZ-10-CN exhibited the highest intensity as compared to that of its individual constituents, which validates the higher  $\text{OH}^{\cdot}$  radical generation ability of the composite. Additionally, from the NBT test, superoxide radical ions yield formazan derivatives in the reaction mixture, and the photo-generated  $\text{O}_2^{\cdot-}$  decreases the absorption maxima of NBT molecules at 280 nm. The decrease in  $\lambda_{\text{max}}$  at 280 nm indicates that  $\text{O}_2^{\cdot-}$  generation has occurred (Fig. 9b).

By examining the band edge positions and radical-trapping experiments, two possible charge transfer mechanisms can be considered: direct Z-scheme or type-II heterojunction. The traditional type-II heterojunction exhibits a band-to-band carrier transfer mechanism, where the electrons on the CB of  $g\text{-C}_3\text{N}_4$  should migrate to the CB of TNZ-10 to produce  $\text{O}_2^{\cdot-}$  as anticipated, whereas the holes should migrate from the VB of TNZ-10 to the VB of  $g\text{-C}_3\text{N}_4$ . The resultant potentials of both electrons and holes after the separation and migration are not potentially favorable to produce  $\text{O}_2^{\cdot-}$  and  $\text{OH}^{\cdot}$ . However, the direct z-scheme arrangement of the TNZ-10-CN composite suggests that the electrons in the CB of TNZ-10 will tunnel through the junction to combine with the holes of  $g\text{-C}_3\text{N}_4$  so that the resultant holes and electrons will gather at the VB of TNZ-10 and CB of  $g\text{-C}_3\text{N}_4$ , respectively.

From the transient photocurrent and EIS study, it is evident that the presence of N as a surface species ( $\text{NO}_x$ ) increases the

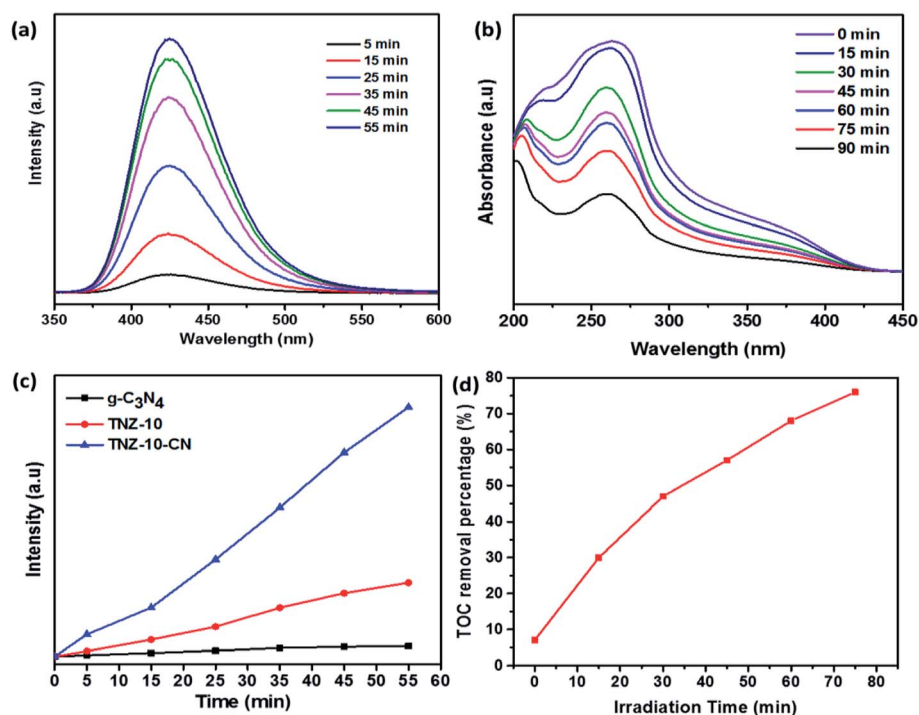


Fig. 9 (a) Terephthalic acid testing, (b) NBT testing for superoxide quantification, (c) comparative PL intensities of 2-hydroxy terephthalic acid using different samples, and (d) the TOC removal percentage of 20 ppm bromoxynil using the active TNZ-10-CN catalyst.

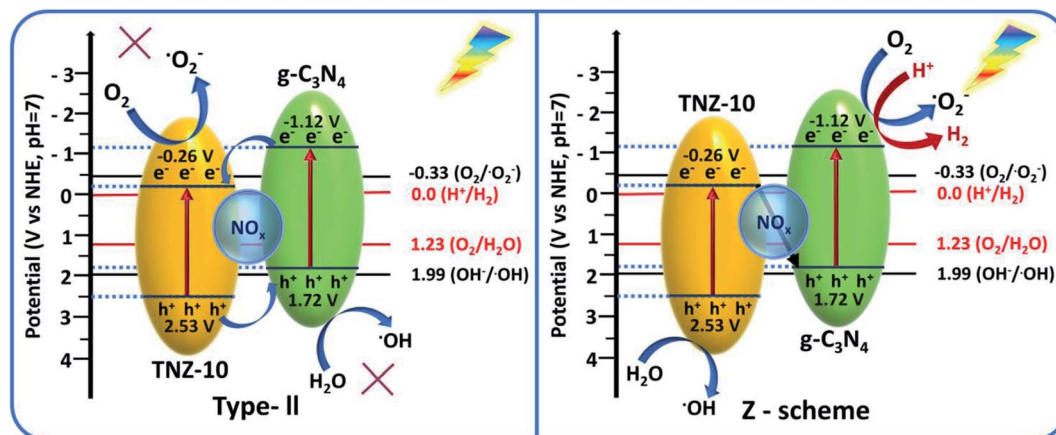
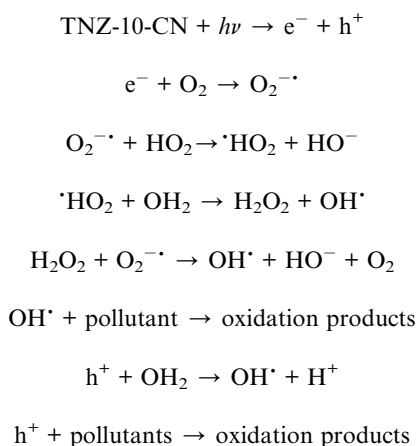


Fig. 10 A schematic presentation of the band structure and probable degradation mechanism.

electron-hole recombination at the depletion region, and provides a satisfactory agreement for the z-scheme mechanism. The inbuilt field developed in the depletion region can boost the recombination process of carriers, which facilitates the z-scheme mechanism for the photocatalytic process. As per the z-scheme representation, the gathered photo-generated electrons possess high reducibility ( $-1.12$  V vs. NHE) that can easily reduce dissolved  $O_2$  to  $O_2^{\cdot-}$  ( $-0.33$  V vs. NHE) along with the generation of  $H_2$  from  $H^+$  ( $0.0$  V vs. NHE) in the same aquatic environment. The residual holes at the VB edge of TNZ-10 possess the appropriate potential ( $2.53$  V vs. NHE) to produce  $OH^{\cdot}$ , which indicates the probability of a direct z-scheme mechanism. By considering the relative band edge position of the heterostructure and the relative standard redox potential of the active species  $OH^{\cdot}$  ( $1.99$  V vs. NHE) and  $O_2^{\cdot-}$  ( $-0.33$  V vs. NHE), the following reaction pathway can be considered:



The photo-induced holes accumulated in the VB edge of pure TNZ-10 are able to produce  $OH^{\cdot}$  radicals from  $OH^-$  in the reaction mixture, while the electrons in  $g\text{-C}_3\text{N}_4$  are able to produce  $O_2^{\cdot-}$  radicals from dissolved  $O_2$ . If the catalyst had followed the conventional band-to-band charge transfer mechanism (conventional type-II heterojunction), the generation of the active species would not have been possible. The reactive species ( $OH^{\cdot}$

and  $O_2^{\cdot-}$ ) were compiled on the active sites of the photocatalyst, and were able to participate in the degradation process. Regarding  $H_2$  evolution, after overall charge separation and migration through the z-scheme, the resultant electrons compiled on the CB of  $g\text{-C}_3\text{N}_4$  ( $-1.12$  V vs. NHE) are at a favorable potential to undergo the hydrogen evolution reaction ( $0.0$  V vs. NHE) using methanol as a hole scavenger (Fig. 10).

## 4. Conclusions

This work successfully tailored the band edge of  $TiO_2$  by doping Zr *via* substantially replacing Ti from its lattice point, as doping creates defect levels below the conduction band by reducing the overall band threshold. Co-doped N was fabricated as a surface species, which enhanced the carrier mobility throughout the surface and resulted in a preference for the recombination process at the depletion region with  $g\text{-C}_3\text{N}_4$ , in support of a z-scheme mechanism. To counterbalance the recombination process of individual materials (a consequence of the defect level), heterojunctions were fabricated over  $g\text{-C}_3\text{N}_4$  *via* a simple co-calcination method. Physicochemical evaluation revealed an intimate architecture, suitable band edge position, low interfacial charge resistance, and a reduced rate of recombination that synergistically enhanced the photocatalytic  $H_2$  generation along with the degradation process. Moreover, the redox potentials of the resultant carriers were able to generate both  $OH^{\cdot}$  and  $O_2^{\cdot-}$  through a direct z-scheme mechanism, participating in the degradation of bromoxynil.

## Conflicts of interest

There are no conflicts to declare.

## Acknowledgements

The authors are thankful to the Science and Engineering Research Board, SERB, India for funding this research project (EMR/2017/000406). The authors are also thankful to the



National Institute of Technology, Rourkela for providing the instrumental facilities.

## References

- 1 W. J. Ong, L. L. Tan, Y. H. Ng, S. T. Yong and S. P. Chai, *Chem. Rev.*, 2016, **116**, 7159–7329.
- 2 X. Li, J. Yu and M. Jaroniec, *Chem. Soc. Rev.*, 2016, **45**, 2603–2636.
- 3 J. Liu, Y. Liu, N. Liu, Y. Han, X. Zhang, H. Huang, Y. Lifshitz, S. T. Lee, J. Zhong and Z. Kang, *Science*, 2015, **347**, 970–974.
- 4 X. Liu, J. Iocozzia, Y. Wang, X. Cui, Y. Chen, S. Zhao, Z. Li and Z. Lin, *Energy Environ. Sci.*, 2017, **10**, 402–434.
- 5 Y. Li, Y. Bian, H. Qin, Y. Zhang and Z. Bian, *Appl. Catal., B*, 2017, **206**, 293–299.
- 6 W. H. Leng, P. R. F. Barnes, M. Juozapavicius, B. C. O'Regan and J. R. Durrant, *J. Phys. Chem. Lett.*, 2010, **1**, 967–972.
- 7 D. Chatterjee and A. Mahata, *J. Photochem. Photobiol., C*, 2005, **6**(2–3), 186–205.
- 8 D. Chatterjee and S. Dasgupta, *J. Photochem. Photobiol., C*, 2005, **6**, 186–205.
- 9 H. Liu, G. Liu and X. Shi, *Colloids Surf., A*, 2010, **363**, 35–40.
- 10 H. Hou, M. Shang, F. Gao, L. Wang, Q. Liu, J. Zheng, Z. Yang and W. Yang, *ACS Appl. Mater. Interfaces*, 2016, **8**, 20128–20137.
- 11 J. Yang, X. Wang, J. Dai and J. Li, *Ind. Eng. Chem. Res.*, 2014, **53**, 12575–12586.
- 12 K. Li, S. Gao, Q. Wang, H. Xu, Z. Wang, B. Huang, Y. Dai and J. Lu, *ACS Appl. Mater. Interfaces*, 2015, **7**, 9023–9030.
- 13 S. J. A. Moniz, S. A. Shevlin, D. J. Martin, Z. X. Guo and J. Tang, *Energy Environ. Sci.*, 2015, **8**, 731–759.
- 14 J. Fu, J. Yu, C. Jiang and B. Cheng, *Adv. Energy Mater.*, 2018, **8**, 1–31.
- 15 J. Zhang, X. Jin, P. I. Morales-Guzman, X. Yu, H. Liu, H. Zhang, L. Razzari and J. P. Claverie, *ACS Nano*, 2016, **10**, 4496–4503.
- 16 Z. Huang, Q. Sun, K. Lv, Z. Zhang, M. Li and B. Li, *Appl. Catal., B*, 2015, **164**, 420–427.
- 17 H. Yan and H. Yang, *J. Alloys Compd.*, 2011, **509**, 26–29.
- 18 R. Guo, D. Zeng, Y. Xie, Y. Ling, D. Zhou, L. Jiang, W. Jiao, J. Zhao and S. Li, *Int. J. Hydrogen Energy*, 2020, **45**, 22534–22544.
- 19 Y. Wang, X. Ding, P. Zhang, Q. Wang, K. Zheng, L. Chen, J. Ding, X. Tian and X. Zhang, *Ind. Eng. Chem. Res.*, 2019, **58**, 3978–3987.
- 20 S. Chen, Y. Qi, T. Hisatomi, Q. Ding, T. Asai, Z. Li, S. S. K. Ma, F. Zhang, K. Domen and C. Li, *Angew. Chem., Int. Ed.*, 2015, **54**, 8498–8501.
- 21 R. Hao, G. Wang, H. Tang, L. Sun, C. Xu and D. Han, *Appl. Catal., B*, 2016, **187**, 47–58.
- 22 J. Yan, H. Wu, H. Chen, Y. Zhang, F. Zhang and S. F. Liu, *Appl. Catal., B*, 2016, **191**, 130–137.
- 23 W. K. Jo and T. S. Natarajan, *Chem. Eng. J.*, 2015, **281**, 549–565.
- 24 W. K. Jo and N. C. S. Selvam, *Chem. Eng. J.*, 2017, **317**, 913–924.
- 25 D. Ma, J. Wu, M. Gao, Y. Xin and C. Chai, *Chem. Eng. J.*, 2017, **316**, 461–470.
- 26 Q. Wang, Y. Li, T. Hisatomi, M. Nakabayashi, N. Shibata, J. Kubota and K. Domen, *J. Catal.*, 2015, **328**, 308–315.
- 27 G. C. Wessler, T. Zhu, J. P. Sun, A. Harrell, W. P. Huhn, V. Blum and D. B. Mitzi, *Chem. Mater.*, 2018, **30**, 6566–6574.
- 28 P. Zhang, Y. Yu, E. Wang, J. Wang, J. Yao and Y. Cao, *ACS Appl. Mater. Interfaces*, 2014, **6**, 4622–4629.
- 29 L. Ye, J. Liu, Z. Jiang, T. Peng and L. Zan, *Appl. Catal., B*, 2013, **142–143**, 1–7.
- 30 V. S. Santosh Kumar, T. Surendar, B. Kumar and A. Baruah, *J. Phys. Chem. C*, 2013, **8**, 4284–4294.
- 31 P. D. Cozzoli, A. Kornowski and H. Weller, *J. Am. Chem. Soc.*, 2003, **125**, 14539–14548.
- 32 X. Wang, K. Maeda, X. Chen, K. Takanabe, K. Domen, Y. Hou, X. Fu and M. Antonietti, *J. Am. Chem. Soc.*, 2009, **131**, 1680–1681.
- 33 X. Wang, K. Maeda, A. Thomas, K. Takanabe, G. Xin, J. M. Carlsson, K. Domen and M. Antonietti, *Nat. Mater.*, 2009, **8**, 76–80.
- 34 J. Macan, A. Gajović and H. Ivanković, *J. Eur. Ceram. Soc.*, 2009, **29**, 691–696.
- 35 W. F. Zhang, Y. L. He, M. S. Zhang, Z. Yin and Q. Chen, *J. Phys. D: Appl. Phys.*, 2000, **33**, 912–916.
- 36 Y. Nan, D. Yang, Z. Tong, Y. Sun and Z. Jiang, *Mater. Res. Bull.*, 2017, **93**, 91–101.
- 37 J. Hong, X. Xia, Y. Wang and R. Xu, *J. Mater. Chem.*, 2012, **22**, 15006–15012.
- 38 Y. Choi, H. Il Kim, G. H. Moon, S. Jo and W. Choi, *ACS Catal.*, 2016, **6**, 821–828.
- 39 J. Wang, Y. Yu, S. Li, L. Guo, E. Wang and Y. Cao, *J. Phys. Chem. C*, 2013, **117**, 27120–27126.
- 40 X. Song, Y. Hu, M. Zheng and C. Wei, *Appl. Catal., B*, 2016, **182**, 587–597.
- 41 W. J. Ong, L. L. Tan, S. P. Chai and S. T. Yong, *Chem. Commun.*, 2015, **51**, 858–861.
- 42 S. Zhou, Y. Liu, J. Li, Y. Wang, G. Jiang, Z. Zhao, D. Wang, A. Duan, J. Liu and Y. Wei, *Appl. Catal., B*, 2014, **158–159**, 20–29.
- 43 Z. Bastl, A. I. Senkevich, I. Spirovová and V. Vrtílková, *Surf. Interface Anal.*, 2002, **34**, 477–480.
- 44 Z. Wei, F. Liang, Y. Liu, W. Luo, J. Wang, W. Yao and Y. Zhu, *Appl. Catal., B*, 2017, **201**, 600–606.
- 45 J. Zhou, T. Li, Z. Shu, Y. Tan, Z. Zhao and W. Wang, *Appl. Catal., B*, 2018, **230**, 260–268.
- 46 J. Long, H. Chang, Q. Gu, J. Xu, L. Fan, S. Wang, Y. Zhou, W. Wei, L. Huang, X. Wang, P. Liu and W. Huang, *Energy Environ. Sci.*, 2014, **7**, 973–977.
- 47 C. Li, Z. Lou, Y. Yang, Y. Wang, Y. Lu, Z. Ye and L. Zhu, *Langmuir*, 2019, **35**, 778–786.
- 48 A. S. Dezfuli, M. R. Ganjali, H. R. Naderi and P. Norouzi, *RSC Adv.*, 2015, **5**, 46050–46058.
- 49 T. Giannakopoulou, I. Papailias, N. Todorova, N. Boukos, Y. Liu, J. Yu and C. Trapalis, *Chem. Eng. J.*, 2017, **310**, 571–580.
- 50 D. Xu, B. Cheng, S. Cao and J. Yu, *Appl. Catal., B*, 2015, **164**, 380–388.

- 51 J. Luo, X. Zhou, L. Ma and X. Xu, *Rational Construction of Z-Scheme  $\text{Ag}_2\text{CrO}_4/\text{g-C}_3\text{N}_4$  Composites with Enhanced Visible-Light Photocatalytic Activity*, Elsevier B.V., 2016, vol. 390.
- 52 S. Sakthivel and H. Kisch, *Angew. Chem., Int. Ed.*, 2003, **42**, 4908–4911.
- 53 P. Chelme-Ayala, M. G. El-Din and D. W. Smith, *Water Res.*, 2010, **44**, 2221–2228.
- 54 Z. Tong, D. Yang, T. Xiao, Y. Tian and Z. Jiang, *Chem. Eng. J.*, 2015, **260**, 117–125.
- 55 H. Zhu, D. Chen, D. Yue, Z. Wang and H. Ding, *J. Nanopart. Res.*, 2014, **16**, 1–10.
- 56 Y. Chen, W. Huang, D. Hem, S. Yue and H. Huang, *ACS Appl. Mater. Interfaces*, 2014, **84**, 203–211.
- 57 B. Zhang, Q. Wang, J. Zhuang, S. Guan and B. Li, *J. Photochem. Photobiol., A*, 2018, **362**, 1–13.
- 58 J. Ma, X. Tan, T. Yu and X. Li, *Int. J. Hydrogen Energy*, 2016, **41**, 3877–3887.
- 59 D. Yang, X. Zhao, Y. Chen, W. Wang, Z. Zhou, Z. Zhao and Z. Jiang, *Ind. Eng. Chem. Res.*, 2019, **58**, 5516–5525.